RESEARCH ARTICLE

**ADVANCED
PHOTONICS
RESEARCH**
Open Access

www.adpr-journal.com

Second-Order Optical Response in Electrically Polarized Sodo-Niobate Amorphous Thin Films: Particularity of Multilayer Systems

Lara Karam, Frédéric Adamietz, Dominique Michau, Ganapathy Senthil Murugan, Thierry Cardinal, Evelyne Fargin, Vincent Rodriguez, Kathleen A. Richardson, and Marc Dussauze*

Herein, our attention is focused on the second-order optical properties of thermally poled sodo-niobate amorphous thin films through an original methodology that combines both macroscopic and microscopic second harmonic generation techniques. By probing the geometry and the magnitude of the second-order nonlinear (SONL) optical response at different scales, a key aspect of thin film's poling mechanisms compared with bulk glasses is demonstrated that lies in the appearance of a charge accumulation at the film/substrate interface and that is described by the Maxwell–Wagner effect. A way to minimize this effect is then proven by promoting an induced built-in static field in the plane of the film using a microstructured electrode. A SONL optical susceptibility as high as $29 \, \text{pm} \, \text{V}^{-1}$ is measured and its geometry and location are controlled at the micrometer scale; it constitutes an improvement of at least one order of magnitude compared with other poled amorphous inorganic materials and is comparable with that of lithium niobate single crystal.

1. Introduction

The domain of photonic integrated circuits (PICs) constantly seeks for new materials and processes to face its current challenges in particular when it comes to miniaturization and multifunctionality. Many active optical devices such as electrooptical modulators or frequency convertors rely on second-order nonlinear (SONL) optical properties. Current devices are based on dielectric crystalline materials, including lithium niobate ($LiNbO_3$), lithium tantalite ($LiTaO_3$), potassium titanyl phosphate ($KTiOPO_4$), and semiconductors such as GaAs. In particular, lithium niobate is a good platform for active optical devices for telecommunications as this crystal exhibits strong SONL response ($\chi_{zzz}^{(2)} = 55 \, \text{pm} \, \text{V}^{-1}$ for the single crystal grown from the congruent melt)[1] and a good optical transparency from the visible to the mid-infrared.[2–4] However, important geometry constrains inherent to the crystallinity of this material exist along with important fabrication costs. Amorphous materials are cheaper, more flexible, and versatile in the sense that they can be made through a wide range of forming processes and do not present geometry constrains due to their isotropic nature. However, they do not present SONL properties due to their centrosymmetric structure. Nevertheless, it is now well known that processes such as thermal poling can break this symmetry to induce a SONL response in amorphous materials. The basic principle of this

Dr. L. Karam, F. Adamietz, Prof. V. Rodriguez, Dr. M. Dussauze
Institut des Sciences Moléculaires
UMR 5255 CNRS
Université de Bordeaux
351 Cours de la Libération, Talence Cedex 33405, France
E-mail: marc.dussauze@u-bordeaux.fr

D. Michau, Dr. T. Cardinal, Prof. E. Fargin
Institut de Chimie de la Matière Condensée de Bordeaux
UMR 5026 CNRS
Université de Bordeaux
87 avenue du Dr. Albert Schweitzer, Pessac Cedex 33600, France

Dr. G. S. Murugan
Optoelectronics Research Centre
University of Southampton
Southampton SO17 1BJ, UK

Prof. K. A. Richardson
CREOL
College of Optics and Photonics
Department of Materials Science and Engineering
University of Central Florida
Orlando, FL 32816, USA

process is simple and has been applied to glasses to produce a SONL response since the beginning of the 1990s.[5] Thermal poling of a large variety of glass families has been examined, including all types of pure silica,[5–8] silicate,[9–12] phosphate,[13–16] germanate,[17,18] tellurite,[19–21] and chalcogenide[22,23] materials, with this list being nonexhaustive. Various attempts have been made to develop optical devices relying on the SONL response of poled glasses with the glasses being either in the form of optical fibers[24,25] or in planar systems.[26–28] However, at this stage, SONL responses of poled glasses have typically been found to be too low to compete with crystalline materials.

Recently, we have proposed a new approach to address this issue, consisting of: 1) the development of new amorphous thin film optical materials whose composition lies outside of the classical glass forming regions, prepared using radio frequency (RF) sputtering deposition of sodium niobate compositions[29] and 2) a thermoelectrical imprinting process using structured electrodes demonstrating control at the micrometer scale of the localization and the geometry of the induced anisotropy.[23,29,30] These sodo-niobate amorphous thin films have been found to be particularly well adapted to the thermal poling process as they exhibit second-order optical susceptibilities ($\chi^{(2)}$) greater than 20 pm V^{-1} corresponding to an improvement of one order of magnitude as compared with poled glassy systems and being now close to the targeted property of lithium niobate.[29]

Following this promising result, we propose to investigate here the peculiarities of a thermoelectrical process on amorphous thin films. To this end, we combine two second harmonic generation (SHG) metrology tools to quantify and clarify 1) the origin of the second-order optical nonlinearity and 2) to describe its geometry and localization in the poled films. The objectives here consist of confirming and advancing the understanding of the creation of the high poling-induced SONL response exhibited by these new amorphous optical materials as well as providing new insights for their future integration.

2. Results

2.1. Electrode Design and Thermal Poling Efficiency

In the current work, the anode consists of an indium tin oxide (ITO) thin film deposited on a glass slide. The ITO can be removed locally by laser ablation to generate structures (alternating conductive/nonconductive areas following a specific pattern).[30] As shown in **Figure 1**a, we chose to divide the electrode into two different zones: 1) the homogeneous zone (the electrode is everywhere conductive) and 2) the structured zone (ITO is ablated over lines of different widths). This allows one to study, on a single sample, the effect of thermal poling under two different electric field geometries. Indeed, as shown in Figure 1b, in the homogenous zone, the field lines during the process are perpendicular to the plane of the sample (i.e., along the Z-axis), while in the structured zone, an in-plane component appears (i.e., components along the X-axis as well as the Z-axis).

This electrode was used to pole four thin films exhibiting different thicknesses—1.8, 1.5, 1.0, and 0.5 μm, respectively. We will first focus our interest on the thickest film of this selection
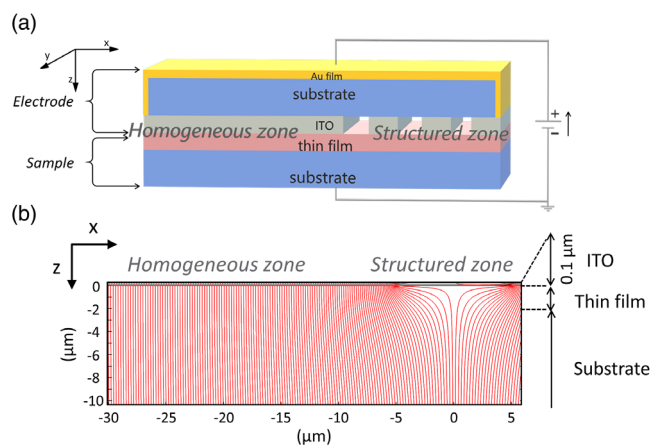
Figure 1. a) Schematic of the sample and the electrode during thermal poling. The electrode is constituted of two different zones: homogeneous and structured zones. b) Calculated electric field lines (in red) applied by the electrode during the process in the two aforementioned regions.

and on the effect of poling in the homogeneous zone. The poling efficiency in the structured zone has been reported and discussed in a previous study.[29]

The Raman spectra acquired on the cross section of the film prior to and after the poling treatment are shown in **Figure 2**a. Prior to poling, two distinct contributions can be observed in the Raman response: the first band is centered on 660 cm^{-1} and the second one on 840 cm^{-1}. In the region between 600 and 1000 cm^{-1}, the Nb—O stretching modes can be found.[31] Between 600 and 750 cm^{-1}, the Nb—O—Nb bonds connecting NbO$_6$ octahedrons in a 3D network are found; at 600 cm^{-1}, the network is perfectly regular just like in NaNbO$_3$ perovskite,[32] while a response at higher wavenumbers indicates a distortion of the network. The second band at 840 cm^{-1} corresponds to distorted octahedrons Nb—O bond certainly induced by the sodium cations insertion within the niobate network.[30] A distinct decrease in the band related to sodium is observed in the postpoling spectrum, while the band related to the 3D niobate network is slightly shifted to higher wavenumbers (670 cm^{-1}). The postpoling Raman response of the film is similar to that of amorphous Nb$_2$O$_5$[33] except for the appearance of a band at 1550 cm^{-1}. This band is attributed to molecular oxygen trapped in the glassy matrix and linked to charge compensation mechanisms occurring during poling in a closed anode configuration.[9,11,17] The departure of sodium from the thin film upon poling, suggested by the Raman measurements, is also confirmed by the secondary ion spectrometry (SIMS) profiles measured after poling (Figure 2b). One can observe in these profiles that not only has the whole film's thickness been depleted of sodium, but also a 1.6 μm-thick layer in the substrate is left sodium-depleted after poling. It follows that in the poling conditions considered both the film and the substrate are poled. These considerations confirm the efficiency of the homogeneous thermal poling treatment on the thin film. Overall, the effect of the poling treatment in the homogeneous zone in terms of structure and composition is similar to the one that was previously reported in the structured zone.[29]
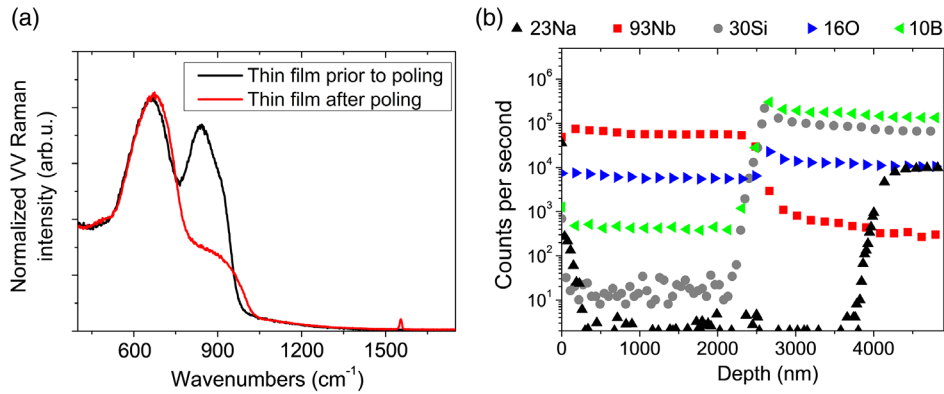
Figure 2. Influence of poling on the structure and composition in the homogeneous zone: a) Raman spectra measured on the cross section of the 1.8 µm-thick film (incident and analyzed polarizations perpendicular to the thin film's surface) prior to (in black) and after thermal poling (in red). b) SIMS measured in the depth of the same thin film after poling.

2.2. Second-Order Optical Response

Two types of complementary measurements were used to probe the SHG response to probe variations over different length scales: 1) the Maker fringe technique, which is a macroscopic transmission technique, is used in the homogeneous zone and 2) specular reflection SHG microscopy allows probing the response both in the homogenous and structured zones. In the schematic of **Figure 3**, the probed volumes are represented in yellow. On the one hand, in the Maker fringe configuration, the whole sample's thickness is probed (thicker than the coherence length, L_C). On the other hand, in the reflection microscopy setup, only a thickness of λ is probed (see Experimental Section); that is a thickness smaller than the coherence length. In this second setup, three different incident polarizations are used, namely, linear, radial, and azimuthal polarizations.
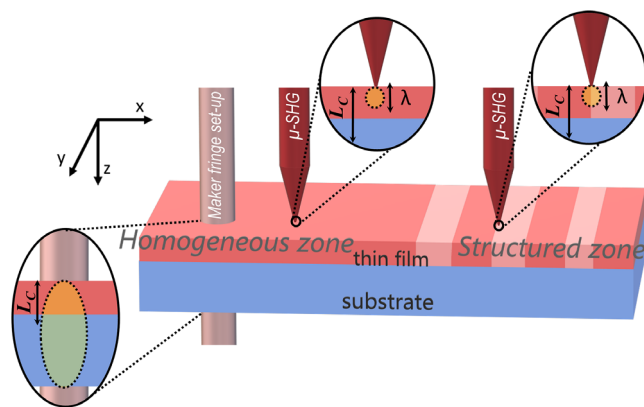
Figure 3. Schematic of the different technics used to probe the second-order response of the postpoling sample. The transmission Maker fringe setup is used in the homogenous zone and the specular reflection SHG microscopy (µ-SHG) is used in the two zones. The probed volumes are represented in yellow. In the transmission Maker fringe configuration, the whole sample's thickness is probed; in the reflection µ-SHG configuration, only the reflection from the air/film interface is collected and a thickness of one wavelength (λ) participate to the SHG (smaller than L_C).

2.2.1. Response in the Homogenous Zone

As mentioned earlier, the simulations presented in Figure 1b show that the electrical constrain in the homogeneous zone is purely along the Z-axis. It follows that the symmetry of the poled glass is $C_{\infty v}$. In the case of SHG, assuming Kleinman's approximation is valid,[34,35] the second-order susceptibility' tensor presents only two independent components and can be expressed as

$$\chi^{(2)} = \begin{bmatrix} 0 & 0 & 0 & 0 & \chi^{(2)}_{zxx} & 0 \\ 0 & 0 & 0 & \chi^{(2)}_{zxx} & 0 & 0 \\ \chi^{(2)}_{zxx} & \chi^{(2)}_{zxx} & \chi^{(2)}_{zzz} & 0 & 0 & 0 \end{bmatrix} \qquad (1)$$

The second-order polarization vector is

$$P^{(2)} = \varepsilon_0 \chi^{(2)} EE = \varepsilon_0 \chi^{(2)} \begin{bmatrix} E_x^2 \\ E_y^2 \\ E_z^2 \\ 2E_y E_z \\ 2E_z E_x \\ 2E_x E_y \end{bmatrix} \qquad (2)$$

where ε_0 is the vacuum permittivity.

On the Maker fringe setup, the rotation of the sample and the control of the incident and analyzed polarizations allow probing of all terms of the tensor. On the µ-SHG setup, the signal is analyzed so that $P_x^{(2)}$ is probed; it thus gives

$$P_x^{(2)} = \varepsilon_0 (2\chi^{(2)}_{zxx} E_z E_x) \qquad (3)$$

It follows that, to probe the $\chi^{(2)}_{zxx}$ component, it is necessary to have at the focal point a combination of both E_x and E_z optical field. We thus chose to probe the SHG response in this zone using a radially polarized light (see **Table 1**) as it fulfills this characteristic as shown in the Experimental Section by the point spread functions (PSFs).

Response Probed in Transmission (Maker Fringe Setup): In **Figure 4**, the ψ-scans (SHG response as a function of the incident

Table 1. Terms of the second-order susceptibility's tensor probed by the different incident polarizations in regions where two different electric field constrains were applied.

| Electrical constrain	Incident light polarization	$\chi^{(2)}$ component probed
Along Z-axis (homogeneous zone)	Radial	$\chi^{(2)}_{zxx}$
Along X- and Z-axis (structured zone)	Radial	$\chi^{(2)}_{xxx}, \chi^{(2)}_{xyy}, \chi^{(2)}_{zxx}$
	Azimuthal	$\chi^{(2)}_{xxx}, \chi^{(2)}_{xyy}$
	X-linear	$\chi^{(2)}_{xxx}, \chi^{(2)}_{xyy}, \chi^{(2)}_{zxx}$

Table 2. SHG response in the homogeneous zone evaluated by the Maker fringe technique: fitting parameters (indices at ω and 2ω and the SHG active layer thickness, L) as well as the resulting simulated $\chi^{(2)}_{zzz}$ for the 1.8 μm-thick film and the two bulk glasses references.

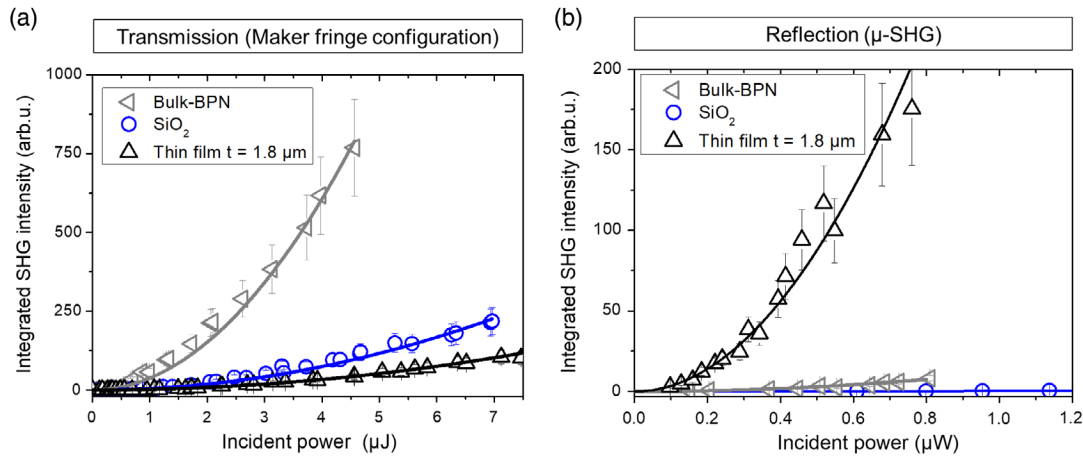|	Thin film ($t = 1.8$ μm)	Bulk-BPN	SiO$_2$
n (1550 nm)	2.033[a]	1.906[b]	1.4440[c]
n (775 nm)	2.076[a]	1.927[b]	1.4538[c]
L [μm]	1.8 ± 0.1	1.9 ± 0.1	4.0 ± 0.5
$\chi^{(2)}_{zzz}$ [pm V^{-1}]	0.80 ± 0.04	3.54 ± 0.18	0.30 ± 0.02

[a]Values extracted from study by Karam et al.;[16] [b]Values extracted from study by Karam et al.;[29] [c]Values extracted from the Heraeus data sheet.

polarization) measured on the film are presented. The θ-scans (see experimental details) are not presented but have been included for the fits. The SHG response is a function of several parameters: the refractive indices at the incident and harmonic wavelengths, the thickness of the SHG active layer (L), the incident intensity, and the second-order susceptibility ($\chi^{(2)}$). The refractive indices were determined in a previous work.[29] The SIMS measurements (Figure 2b) have shown that the whole film's thickness is poled. For the simulations, we have neglected the substrate's contribution to the SHG response and considered that the SHG active layer's thickness was that of the film. The incident intensity is measured during the experiment. These considerations demonstrate the reliability of this technique as the only unknown parameter is $\chi^{(2)}$. The values of the mentioned parameters are shown in **Table 2**.

The obtained fits (continuous lines on Figure 4) overlap well with the experimental points. A value of 0.80 ± 0.04 pm V^{-1} was found for the $\chi^{(2)}_{zzz}$ component of the second-order susceptibility. Furthermore, the ratio $\chi^{(2)}_{zxx}/\chi^{(2)}_{zzz}$ was found to be equal to 1/3; this ratio demonstrates the electrooptic origin of the SHG signal: the measured $\chi^{(2)}$ originates from the interaction of a built-in electric field along the Z-axis (with the referential adopted in this work) and the $\chi^{(3)}$ of an isotropic material.[36]

Two well-known bulk glasses were used as references in this zone: silica (Infrasil)[8] and a bulk borophosphate niobium (Bulk-BPN) glass.[16] Both of them were poled using a homogeneous electrode. Their Maker fringe analysis (data not presented here because similar results were published in our previous works)[8,29] confirmed for both of them the electrooptic origin of the SHG signal. The values of the second-order susceptibilities estimated by this technique as well as the fitting parameters are shown in Table 2. Note that the thickness of the SHG-active layer for these reference samples was evaluated by other means (following the methodology described in our previous work).[16] The only unknown parameter in these fits was the magnitude of the $\chi^{(2)}$, thus making this technique robust. A value of 3.54 ± 0.18 pm V^{-1} was estimated for the Bulk-BPN and one of 0.30 ± 0.02 pm V^{-1} for the silica glass. These values are in agreement with the ones measured in previous works.[8,16]

The SHG responses for the three samples—the film and the two reference materials—as a function of the incident power, are shown in **Figure 5**a. All samples show a quadratic dependence of the SHG with the incident power. In this configuration (macroscopic transmission setup), the response of the poled Bulk-BPN
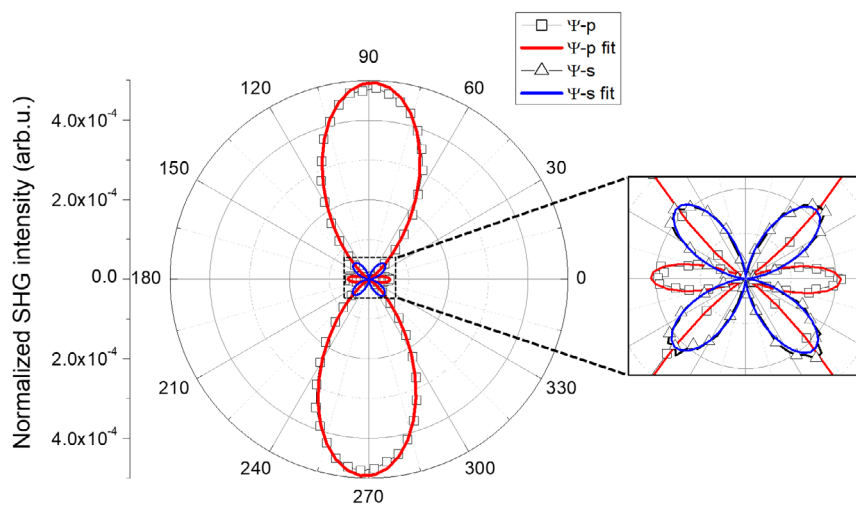
Figure 4. Polarization scans (ψ-scans) measured on the Maker fringe setup of the poled 1.8 μm thick film. The scans correspond to the SHG intensity as a function of the incident polarization. The detection is either p- or s-polarized (ψ-p or ψ-s scans). The opened squares and triangles are the measured points and the continuous lines correspond to a fit with an electrooptic model fit.

**ADVANCED
SCIENCE NEWS**

www.advancedsciencenews.com

**ADVANCED
PHOTONICS
RESEARCH**
Open Access

www.adpr-journal.com

Figure 5. In the homogeneous zone, SHG intensity as a function of the incident power for the two reference bulk glasses (BPN in gray, silica in blue) and the 1.8 μm-thick film measured a) on the Maker fringe transmission setup and b) by specular reflection SHG microscopy (with a radial polarization). The continuous lines correspond to quadratic fits.

is more intense than that of silica and both references present a more intense response than the film's.

Response Probed in Specular Reflection (SHG Microscopy): The film's and references' SHG responses as a function of the incident power as measured by specular reflection microscopy using a radial polarization are shown in Figure 5b. Quadratic laws successfully fit these measurements as illustrated by the continuous lines in the figure. The fitting coefficients, a_{Radial}, for each sample are shown in **Table 3**. In this configuration, the SHG response of the film is one order of magnitude higher than the Bulk-BPN glass' and two orders of magnitude higher that the silica's.

The methodology used to extract the $\chi^{(2)}_{zzz}$ component of a poled glass using a reference of known second-order susceptibility is described in the Experimental Section. To validate this methodology, the Bulk-BPN glass' $\chi^{(2)}_{zzz}$ was estimated using silica as reference. The other way around $\chi^{(2)}_{zzz}$ in silica was also estimated using the Bulk-BPN as a reference. The parameters used in the calculation as well as the calculated values can be found in Table 3. Following this methodology, a value of 3.05 and 0.35 pm V^{-1} was estimated for the Bulk-BPN and silica.
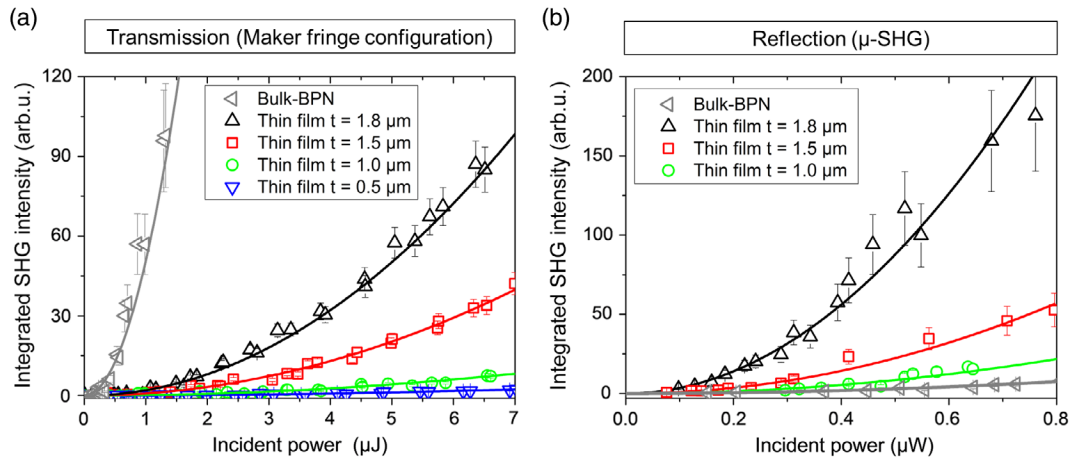
Comparing these values with the ones determined by the Maker fringe technique (Table 2) validates this methodology and allows estimating an error of about 15%.

In a similar manner, the thin film's second-order optical susceptibility as probed in this configuration was estimated using both references. The results are shown in Table 3. A mean value of 20 ± 3 pm V^{-1} is measured in the homogeneous zone of the poled film in a reflection configuration.

Influence of the Film's Thickness: The same methodology was applied to the other films that exhibit smaller thicknesses. **Figure 6** shows the side-by-side evaluation of the SHG response in the homogeneous zone for all films, in the Maker fringe setup configuration (Figure 6a) and in the microscopic specular reflection configuration (Figure 6b). For comparison, the response of the Bulk-BPN reference glass is also presented in these figures.

In the macroscopic transmission configuration, similar to what was observed in Figure 6a, the response of the reference bulk glass is more intense than that of the films. The SHG response intensity decreases when the film's thickness decreases. The fitting coefficients, defined as $a_{\text{Maker fringe}}$, were extracted; they can be found in **Table 4**. From these coefficients, the second-order susceptibility measured in this configuration was estimated for the three other films (with respective thicknesses 1.5, 1.0, and 0.5 μm) using the thicker film as a reference. We took care to account for the difference in thickness for theses estimations. The second-order susceptibilities' values are shown in Table 4. The measured $\chi^{(2)}_{zzz}$ components are comprised between 0.8 ± 0.1 pm V^{-1} for the 1.8 μm-thick film and 0.4 ± 0.05 pm V^{-1} for the two thinner films; that is, in absolute value, a decrease of 0.4 pm V^{-1} from the thicker to the thinner film.

In the microscopic specular reflection configuration, where the SHG response is probed under a radial polarization, the response of the reference glass is lower than that of the films. The film's SHG response decreases when the film's thickness decreases. One must note that the response of the thinner film (0.5 μm) does not appear in Figure 6b. Indeed, on this sample, the power required to obtain an SHG response high enough to be

Table 3. SHG response in the homogeneous zone evaluated by SHG microscopy with a radial polarization: indices at ω and 2ω, coherence length (L_C), quadratic fitting coefficient (from Figure 4b) and evaluated $\chi^{(2)}_{zzz}$ using either bulk glasses references.

	Thin film ($t = 1.8$ μm)	Bulk-BPN	SiO$_2$
n (1064 nm)	2.050[a]	1.916[b]	1.4496[c]
n (532 nm)	2.131[a]	1.969[b]	1.4609[c]
L_C [μm]	3.3	5.0	23.5
a_{Radial}	350	11.69	0.305
$\chi^{(2)}_{zzz}$ with SiO$_2$ as reference [pm V^{-1}]	19 ± 3	3.05 ± 0.50	–
$\chi^{(2)}_{zzz}$ with Bulk-BPN as reference [pm V^{-1}]	22 ± 3	–	0.35 ± 0.05

[a]Values extracted from the study by Karam et al.;[16] [b]Values extracted from study by Karam et al.;[29] [c]Values extracted from the Heraeus data sheet.

Figure 6. Effect of the film's thickness on the second-order optical response. In the homogeneous zone, SHG intensity as a function of the incident power for the films of different thicknesses measured a) on the Maker fringe transmission setup and b) by specular reflection SHG microscopy (with a radial polarization). The measurements of the reference bulk BPN glass are also presented (in gray) for comparison. The continuous lines correspond to quadratic fits.

Table 4. SHG response in the homogeneous and structured zone evaluated by the Maker fringe technique and SHG microscopy (with a radial and a linear polarization) for the films of different thicknesses. $a_{\text{Maker fringe}}$, a_{Radial}, and a_{Linear} correspond, respectively, to the quadratic fitting coefficients extracted from Figure 5 and 7.

	Thin film's thickness (t):	$t = 1.8\,\mu m$	$t = 1.5\,\mu m$	$t = 1.0\,\mu m$	$t = 0.5\,\mu m$
Homogeneous zone	$a_{\text{Maker Fringe}}$	2.009	0.813	0.169	0.048
	$\chi^{(2)}_{zzz}$ Maker fringe [pm V^{-1}]	0.8 ± 0.1	0.6 ± 0.1	0.4 ± 0.05	0.4 ± 0.05
	a_{Radial}	350	88	34	–
	$\chi^{(2)}_{zzz}$ Radial [pm V^{-1}]	20 ± 3	10 ± 1.5	6.4 ± 1	≈ 0
Structured zone	a_{Linear}	6.32	2.66	2.03	0.342
	$\chi^{(2)}_{xxx}$ Linear [pm V^{-1}]	29 ± 4	20 ± 3	17 ± 3	$21 \pm 3^{\text{a)}}$

a)Value adjusted to account for the fact that this film is twice thinner than the probed layer.

measured was quite high. The sample was always damaged before enough points were measured. We thus consider that second-order susceptibility induced in this sample is too low to be measured under this configuration. For the three other samples, the quadratic fitting coefficients, a_{Radial}, were extracted (see Table 4). The $\chi^{(2)}_{zzz}$ components were calculated following the methodology previously described and using the Bulk-BPN and the silica poled glasses as references; for each film, the value shown in Table 4 is the mean of these two values. The measured $\chi^{(2)}_{zzz}$ components decrease from 20 to 10 pm V^{-1} between the 1.8 and 1.5 μm-thick films and to 6.4 pm V^{-1} for the 1.0 μm-thick film. It is considered to be close to zero for the thinner film. Overall, in absolute value, that constitutes a decrease of 20 pm V^{-1} from the thicker to the thinner film.

2.2.2. Response in the Structured Zone

In the structured zone, as shown by the simulations displayed in Figure 1b, the electrical constraint exhibits two components: one along the Z-axis and one along the X-axis. The second-order susceptibility tensor can thus be expressed as

$$\chi^{(2)} = \begin{bmatrix} \chi^{(2)}_{xxx} & \chi^{(2)}_{xyy} & \chi^{(2)}_{xyy} & 0 & \chi^{(2)}_{zxx} & 0 \\ 0 & 0 & 0 & \chi^{(2)}_{zxx} & 0 & \chi^{(2)}_{xyy} \\ \chi^{(2)}_{zxx} & \chi^{(2)}_{zxx} & \chi^{(2)}_{zzz} & 0 & \chi^{(2)}_{xyy} & 0 \end{bmatrix} \quad (4)$$

It follows that the analyzed SHG response in this case gives

$$P^{(2)}_x = \varepsilon_0 (\chi^{(2)}_{xxx} E^2_x + \chi^{(2)}_{xyy} E^2_y + \chi^{(2)}_{xyy} E^2_z + 2\chi^{(2)}_{zxx} E_z E_x) \quad (5)$$

More terms are involved in the SHG response than in the homogeneous zone (Equation (3)). It was chosen to use three different probing polarizations, namely, radial, azimuthal, and linear polarizations presenting different nonzero electric field components in the focal region as evidenced by the PSF depicted in the experimental part. These polarizations allow probing different terms of Equation (5); they are shown in Table 1 for the three cases. More specifically, this table illustrates the fact that radially polarized light probes an SHG response originating from an electric field both along the Z-axis and along the X-axis, when the azimuthal polarization only probes terms originating from an electric field along the X-axis.
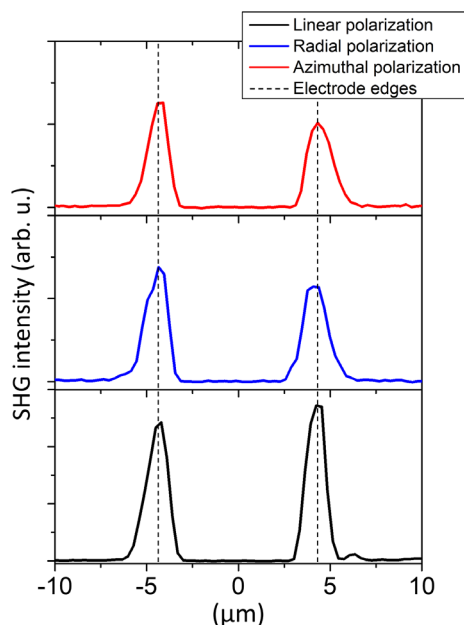
Figure 7. SHG intensity measured across a 9 μm wide line on the poled 1.8 μm-thick thin film probed using different polarizations: in black, with a linear polarization (the sample is oriented so that the linear polarization is perpendicular to the imprinted line); in blue, with a radial polarization; and in red, an azimuthal. The dotted lines correspond to where the electrode edges were during the poling: in between the two dotted line, the ITO was ablated on the electrode.

Figure 7 shows the SHG intensity profiles as probed with linear, radial, and azimuthal polarizations across an imprinted line. The dotted lines on the figure correspond to the electrode edges, meaning the region in between these lines corresponds to the ablated ITO region on the electrode. One can see that the SHG signal as probed with any of three polarizations used is much more intense at the electrode edges than in the rest of the sample. Similarly, for all three polarizations, only one maximum is observed at this location; the SHG intensity then decays in about 3 μm, as previously reported.[29] This behavior is considerably different from the one reported for niobium borophosphate bulk glasses[30] for which the SHG response across an imprinted line presents two maxima when probed under a radially polarized light and one maximum for an azimuthally polarized light. Thereby, in the thin films there is a colocalization of the SHG responses probed with a radial and an azimuthal light. It tends to prove that, in the structured zone, the origin of the SHG signal mainly originates from an electric field along the X-axis (main component probed: $\chi^{(2)}_{xxx}$ for all three polarizations). This is consistent with the uniaxial geometry of the response reported in a previous work on similar poled films.[29]

To quantify the second-order susceptibility in this region, we use a linear polarization and the sample is oriented so that the imprinted line is perpendicular to the incident polarization. Bulk lithium niobate (LiNbO$_3$) grown from congruent melt, oriented so that the linear incident polarization is collinear to its c-axis and its strongest second-order susceptibility coefficient ($\chi^{(2)}_{zzz} = 55 \pm 6$ pm V^{-1})[1] is probed, was used as a reference. Note
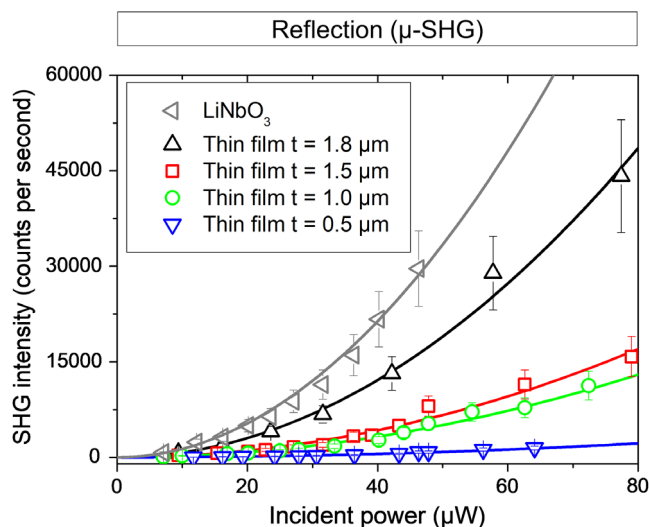
Figure 8. In the structured zone, SHG intensity as a function of the incident power for the films of different thicknesses measured by specular reflection SHG microscopy (with a linear polarization) as well as for the lithium niobate single crystal (in gray) used as a reference. The films are oriented so that the linear polarization is perpendicular to the imprinted line and the lithium niobate crystal is oriented so that its c-axis is collinear to the linear polarization and so that $\chi^{(2)}_{zzz}$ is probed. The continuous lines correspond to quadratic fits. Note that the fitting coefficient corresponding to lithium niobate is 13.36.

that this does not correspond to the phase matching conditions and that there is no propagation in the material (more details in the experimental part). Following the previous methodology, the maximum of the SHG intensity is recorded as a function of the incident intensity; the resulting evolutions are presented for the different films in **Figure 8**. A quadratic law (continuous lines) successfully fits this evolution and the fitting coefficients, a_{Linear}, are shown in Table 4.

The calculated $\chi^{(2)}$ for the films of different thicknesses are shown in Table 4. One can especially note that, in our methodology, we make the assumption that a layer of one wavelength (i.e., 1 μm) contributes to the SHG radiation.[37] Hence, for the thinnest film being twice thinner than this layer, the value of its $\chi^{(2)}$ has been adjusted by a factor of 4 to account for this as the SHG is a function of L^2 (see experimental details). The measured $\chi^{(2)}$ is found to be an exceptionally large value of 29 pm V^{-1} for the thicker film and close (± 3 pm V^{-1}) to 20 pm V^{-1} for the other films.

3. Discussion

In bulk glasses, thermal poling is known to induce a sodium migration under the anode that goes along with structural rearrangements. The SIMS and Raman measurements on the poled films have shown a similar behavior confirming the transferability of this process from bulk to thin film amorphous materials.

In the homogeneous region, the electrooptical origin (built-in electric field along the Z-axis) of the SHG was demonstrated for the films as well as for the bulk glass references. On the bulk materials, equivalence between the macroscopic response in
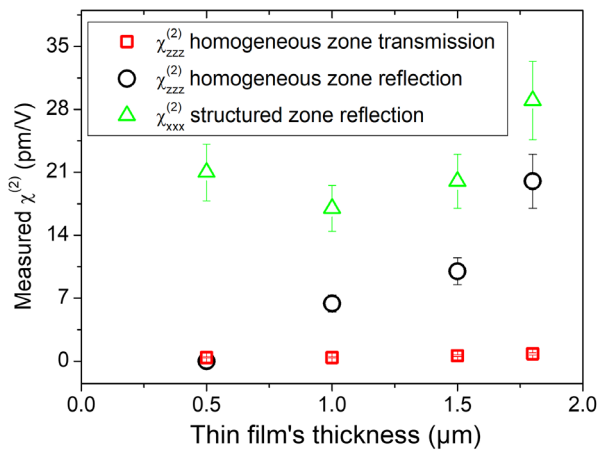
Figure 9. Measured second-order susceptibilities as a function of the film's thickness under the different measurement configurations. The red squares and black circles correspond to the values measured in the homogeneous zone, respectively, on the Maker fringe configuration setup and by specular reflection SHG microscopy (with a radial polarization). The green triangles correspond to the one measured by specular reflection SHG microscopy (with a linear polarization) in the structured zone.

transmission and the microscopic response in reflection was measured; conversely, the films' SHG responses show a major discontinuity between these two configurations. **Figure 9** shows the measured $\chi^{(2)}$ as a function of the films' thickness as measured in transmission and in reflection. On the one hand, the film's thickness has a distinct influence on the second-order susceptibility's magnitude, when probed in reflection with a decrease in its value from 20 to 0 pm V^{-1} from the thicker to the thinner film. On the other hand, its magnitude is low (<1 pm V^{-1}) and rather constant when probed in transmission. This constitutes a specificity of the thin films' thermal poling and cannot be explained by classical electrostatic models describing this treatment.[14]

The Maxwell–Wagner effect describes the charge accumulation at the interface between two materials presenting different charge carriers' relaxation times under an applied voltage. These relaxation times are in fact related to the ratio between the dielectric constant and the conductivity of the materials.[38,39] The case of thermal poling of a thin film deposited on a substrate falls within the scope of this model, as film and substrate exhibit different properties. To understand the effect of a charge accumulation at the film/substrate interface, simulations of the electric field resulting from different charge distributions were performed. These results are shown in **Figure 10**. The postpoling film–substrate stacking was divided into three charged layers as illustrated by the schematic of Figure 10a: a negatively charged layer (fixed charge density) in the film and two positively and negatively charged layers at the interface, respectively. These two layers illustrate the Maxwell–Wagner effect on the film's side of the interface and on the substrate's, respectively. The order of magnitude of the charge densities was estimated in coherence with other works in which the trapped charge densities after poling under a blocking anode were evaluated.[40] The electric field was calculated for different charge densities of the two layers at

the film–substrate interface. Examples of some of these simulations are shown in Figure 10b.

One can observe that, at low charge accumulation at the interface (the black curve in Figure 10b), the electric field induced in the thin film is everywhere negative. When the trapped charge density at this interface increases, a positive electric field also appears in the film and becomes more and more intense. Figure 10c,d shows the two distinct cases of (Figure 10c) a poled bulk glass, without any charge accumulation and (Figure 10d) a poled thin film, with a charge accumulation induced by the Maxwell–Wagner effect. In the bulk glass, the postpoling built-in electric field is negative close to the anode. On the figure, it is represented by the $\vec{E}_{Zclassical}$ vector. In the poled thin film, the built-in electric field is negative close to the anode ($\vec{E}_{Zclassical}$) and positive close to the film/substrate interface. The $\vec{E}_{ZMW}$ vector represents this second electric field, which is induced by the Maxwell–Wagner effect.

The thin film's coherence length, L_C, shown in Table 3 amounts to 3.3 µm. For all the films studied here, it is thus larger than the film's thickness. It follows that the two opposite fields ($\vec{E}_{Zclassical}$ and $\vec{E}_{ZMW}$) are contained in a layer thinner than the coherence length. Consequently, the transmission Maker fringe measurement cannot distinguish between these two opposite contributions. As the electric field induced second harmonic (EFISH) origin of the signal was demonstrated, $\chi^{(2)} = 3\chi^{(3)}.E$ and the measured second-order susceptibility corresponds to the sum of these fields for all the films of different thicknesses. As a result, a weak second-order susceptibility is measured on the Maker fringe setup and it is rather constant for all film's thicknesses.

In contrast, using the specular reflection µ-SHG setup, only the first micron of the sample is probed. It follows that for the thicker film, mainly $\vec{E}_{Zclassical}$ is probed. This explains the drastic difference of second-order susceptibility measured in reflection and in transmission for the thickest film (see Figure 9). The thinner the film is, the more important the contribution of $\vec{E}_{ZMW}$ is. Consequently, the second-order susceptibility measured in this configuration decreases with the film's thickness until it is too low to be measured on the used setup as illustrated by the 0.5 µm-thick film.

In the structured zone, we have demonstrated that the main contribution to the SHG response was originating from an electric field along the X-axis. The evolution of the second-order susceptibility in this zone as a function of the films' thickness is shown in Figure 9. First, one can observe that the measured second-order susceptibility in this zone is higher than the one measured in the homogeneous zone for all films. Second, within the error of the measure its value (≈ 20 pm V^{-1}) can be considered as constant for the three thinner films. The measured second-order susceptibility increases for the thicker film ($t = 1.8$ µm) with a value of 29 ± 4 pm V^{-1}. It follows that contrary to what is observed in the homogeneous zone, the response in the structured zone seems not to be impacted by the Maxwell–Wagner effect. This can be explained by the fact that, as the main contribution to the SHG signal originates from an electric field in the plane, in first approximation, it allows to avoid the effect of the interface. Higher second-order susceptibilities can thus be induced under this poling geometry. In addition, we have confirmed here that the microlocalization and the uniaxial character of this response align with that shown in our previous work.[29]
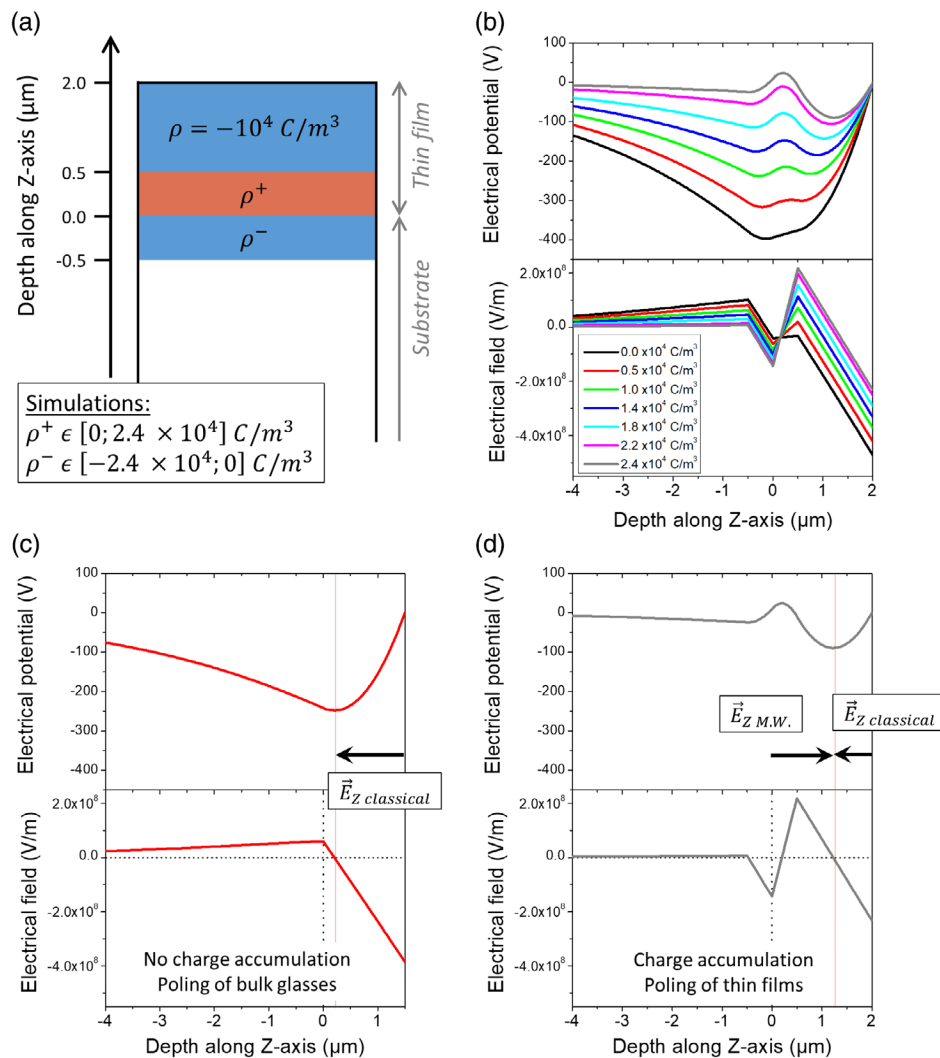
Figure 10. a) Schematic of the electrostatic model describing the charge accumulation at the film/substrate interface in the homogeneously poled thin film. After poling, the film is charged negatively (density fixed to $-10^4\,\mathrm{C\,m^{-3}}$). The charged accumulation described by the Maxwell–Wagner effect is represented by two 0.5 µm-thick layers at the interface—one on the film's side and the other on the substrate—respectively charged positively (ρ^+) and negatively (ρ^-). These charge densities are comprised, in absolute value, between 0 and $2.4 \times 10^4\,\mathrm{C\,m^{-3}}$ (with $0.5 \times 10^4\,\mathrm{C\,m^{-3}}$ steps). For all ρ^+ and ρ^- combinaisons, the electrical potential and electrical fields were calculated. b) Examples of these calculations for several charge distributions with ρ^- fixed to $-10^{-4}\,\mathrm{C\,m^{-3}}$ and ρ^+ varying are presented. c,d) The electrical potential and electric field for two specific charge distributions are presented: c) corresponds to the poling of bulk glasses, i.e., without charge accumulation ($\rho^+ = \rho^- = 0\,\mathrm{C\,m^{-3}}$) and d) to the case of the thin film with a sufficient charge accumulation to explain the observed results ($\rho^+ = 2.4 \times 10^4\,\mathrm{C\,m^{-3}}$, $\rho^- = -1.0 \times 10^4\,\mathrm{C\,m^{-3}}$).

These attributes demonstrate that structured poling could be perfectly adapted to take on the next step with the formation of waveguides from these sodo-niobate thin films in which a strong and microlocalized second-order response can be induced.

4. Conclusion

In conclusion, we have characterized in detail the second-order optical properties of poled sodo-niobate thin films by combining different approaches to measure and clarify the induced SHG using a multiscale length, quantitative approach. One order of magnitude of difference has been observed for the $\chi^{(2)}$ coefficients measured either by a macroscopic or by a microscopic SHG technique. A Maxell–Wagner effect inducing charge accumulations at the film/substrate interface is evoked to explain the experimental measurements. Such effect in the poling mechanisms is specific to the poled thin films for which dielectric constant and conductivity differ from the substrate. It is also shown that one can avoid the Maxwell–Wagner polarization effect by promoting an in-plane poling by the use of patterned electrodes. In such a case, the in-plane-induced second-order nonlinearity appears independent of the film's thickness. Finally, this study clarifies some important aspects of the poling mechanisms for these niobate amorphous thin films which exhibit an unprecedented high SONL optical susceptibility for an amorphous

**ADVANCED
SCIENCE NEWS**
www.advancedsciencenews.com

**ADVANCED
PHOTONICS
RESEARCH**
www.adpr-journal.com

inorganic material. Such optimization of material type and structure demonstrates the suitability of such a candidate for multimaterial planar integration application in the future.

5. Experimental Section

Thin Films Deposition: Thin films were deposited by RF sputtering in a Leybold L560 system on thoroughly cleaned (in isopropanol and ion sputtered with argon for 4 min) Schott Borofloat 33 substrates. The target (75 mm diameter × 3 mm thick, 99.9% pure) of composition 70.8 mol% Nb_2O_5 + 29.2 mol% Na_2O used for that purpose was purchased from Testbourne Ltd. The films were deposited in an argon/oxygen mixture with a gas flow of 47.5 and 2.5 sccm, respectively, under a pressure of 0.4 Pa at a RF power of 100 W. The deposition rate was about 0.29 μm h^{-1}. The substrates were not heated during the deposition.

Thermal Poling: The thin film on a glass substrate, sandwiched between an anode (on the film side) and a silicon wafer at the cathode, was heated at a rate of 15 °C min^{-1} up to 275 °C under vacuum. A microscope cover was placed between the cathode and the sample to preserve the optical quality on this side. After 10 min under nitrogen flow (6 L min^{-1}) to stabilize the temperature, a DC voltage of 1500 V was applied to the sample (at

a rate of 375 V min^{-1}) and was kept on for 30 min time, after which the sample was brought back to room temperature before the DC voltage was turned off. The anode used consisted of a 100 nm layer of ITO deposited on borosilicate glass. The 10 × 5 mm^2 electrode was patterned by laser ablation (see elsewhere for details).[30] In the case of this study, ITO was removed over several straight lines on a part of the electrode (we call this zone "structured zone"), the rest of the electrode was left untouched ("homogeneous zone").

Thin Film's Characterization: Micro-Raman measurements were recorded in backscattering mode on a confocal micro-Raman spectrometer HR800 (Horiba/Jobin Yvon)—also used for the micro-SHG measurements—with a continuous laser operating at 532 nm. The typical resolution of the measures is 2.5 cm^{-1}. The incident and analyzed signals are polarized vertically. SIMS measurements were performed by Mikhail Klimov at the Material Characterization Facility (MCF) at the University of Central Florida (UCF) on PHI Adept 1010 dynamic SIMS system.

Second-Order Optical Measurements—Maker Fringe Setup: The Maker fringe technique is a macroscopic technique (spot size 150 μm) used in transmission. A 1550 nm intracavity optical parametric oscillator nanosecond laser operating at 30 Hz with a maximum impulsion of 100 μJ during a 20 ns pulse was used. Three sets of experiments were performed: θ-scans (changing the incident angle with incident p- or s-polarized light and collecting p-polarized light), ψ-scans (at a fixed incident angle,
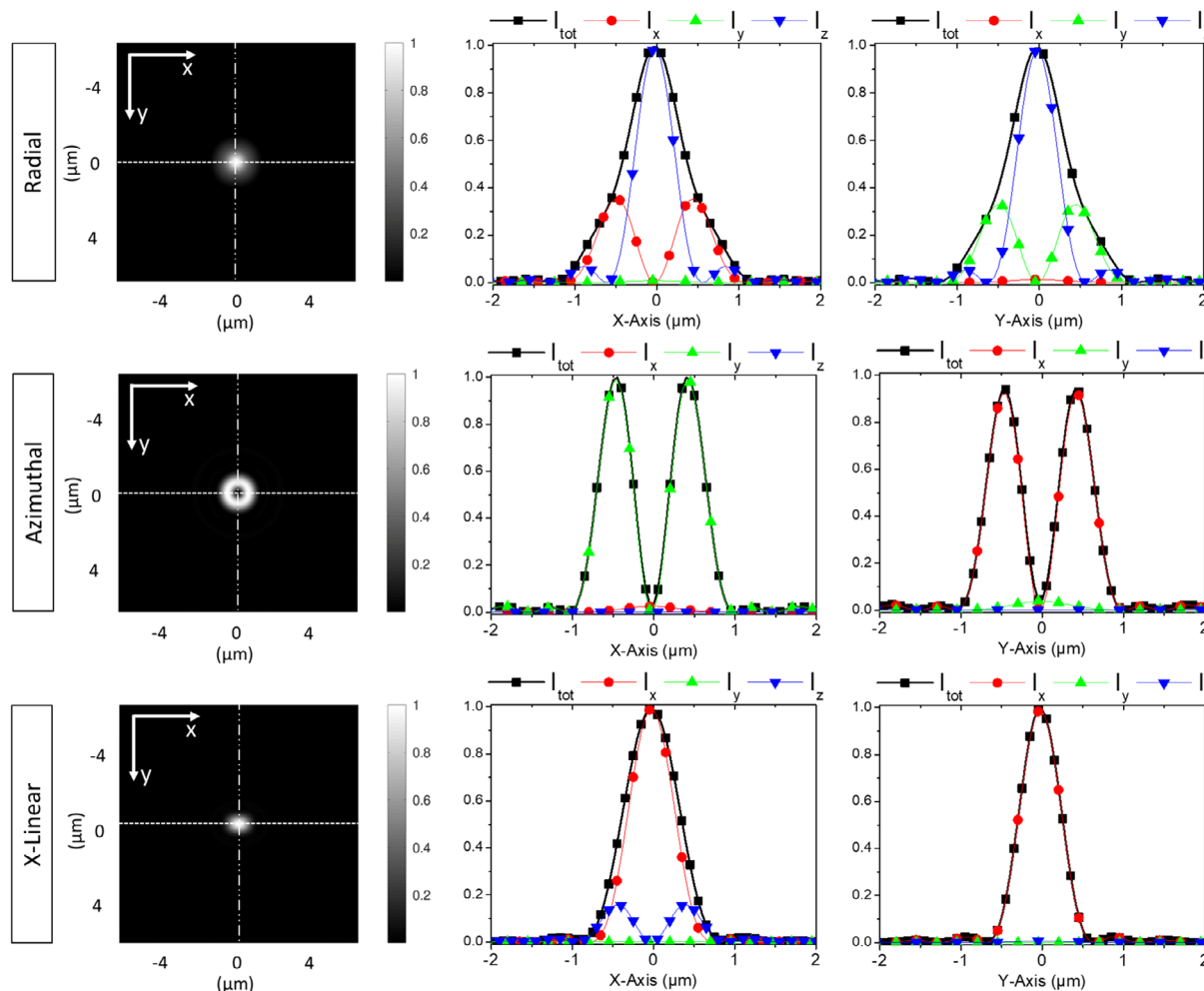
Figure 11. (Left) PSF calculated for a 0.9 numerical aperture and a 1.064 μm wavelength represented in the (X,Y) focal plane for a radial (top), azimuthal (center), and linear (bottom) polarizations. The intensity profiles for each component of the electric field were extracted from the PSF along the X-axis (center) and the Y-axis (right).

changing the incident polarization and collecting p- or s-polarized light), and power scans (with fixed incident angle and fixed incident and analyzed polarizations, changing the incident power). The experiment was calibrated with an α-quartz z-cut plate, which allowed for the determination of absolute values for the second-order susceptibility. The sets of scans were fitted all together using a model described in the study by Rodriguez and Sourisseau.[41]

Second-Order Optical Measurements—Specular Reflection SHG Microscopy: The measurements were performed in backscattering mode on a modified confocal micro-Raman spectrometer HR800 using a picosecond pulsed laser at 1064 nm. Mitutuyo objectives with numerical apertures of 0.42 (50×) and 0.9 (100×) were used, respectively. An *XYZ* stage, with a precision of 0.1 μm, allowed for SHG mapping of the samples. Three incident polarizations can be used: linear, radial, and azimuthal polarizations. The latter two are obtained using a polarization converter from Arcoptix relying on the special alignment of liquid crystal molecules.

To quantify the second-order susceptibility using SHG reflection microscopy in confocal mode, we consider that: 1) only the reflected wave originating from the first interface air/dielectric is collected; 2) one layer of about one wavelength thick ($\approx$1 μm here) contributes to the radiation of the SHG reflected ray as considered by Bloembergen and Pershan.[37] Under these assumptions, as the volume of interaction considered is much lower than the coherence length, it is possible to neglect the classical propagation term in the SHG intensity estimation that can, thus, be written as

$$I_{2\omega} \approx \frac{(2\omega)^2}{8\varepsilon_0 c^3} \frac{|\chi^{(2)}(-2\omega;\omega,\omega)|^2}{n_\omega^2 n_{2\omega}} L^2 I_\omega^2 \qquad (6)$$

We have also considered reflection loss for the incident light; this means the actual intensity that participates to the SHG is

$$I_\omega = \frac{4n_\omega}{(n_\omega + 1)^2} I_\omega^{\text{meas}} \qquad (7)$$

where I_ω^{meas} is the measured intensity before the sample's interface.

Therefore, given these approximations, the SHG reflected intensity can be rewritten as

$$I_{2\omega} \approx \frac{4^2 (2\omega)^2 L^2}{8\varepsilon_0 c^3} \frac{|\chi^{(2)}(-2\omega;\omega,\omega)|^2}{(n_\omega + 1)^4 n_{2\omega}} (I_\omega^{\text{meas}})^2 \qquad (8)$$

If a_{sample} and a_{ref} are, respectively, the fitting coefficient of the quadratic laws for the sample under investigation and for the reference (Bulk-BPN, SiO_2, or $LiNbO_3$), the final expression for the second-order optical susceptibility is

$$\chi_{\text{sample}}^{(2)}(-2\omega;\omega,\omega) = \chi_{\text{ref}}^{(2)}(-2\omega;\omega,\omega) \sqrt{\frac{a_{\text{thin film}}}{a_{\text{ref}}} \frac{n_{2\omega}^{\text{sample}}(n_\omega^{\text{sample}} + 1)^4}{n_{2\omega}^{\text{ref}}(n_\omega^{\text{ref}} + 1)^4}} \qquad (9)$$

PSFs Calculations: The knowledge of the polarization state of light at the focal point is particularly important in this work to understand what terms of the second-order susceptibility's tensor are probed under radial, azimuthal, or linear polarization. This information is given by the PSF that is calculated as a function of the wavelength, the numerical aperture, and the incident polarization by a program written by Li. This program that is running on Octave can be found in the study by Li.[42] The results of these calculations for the three polarization states using in this work are shown in **Figure 11**. They give information on the nonzero components of the incident light electric field in Equation (2).

Acknowledgements

Conflict of Interest

The authors declare no conflict of interest.

Data Availability Statement

The data that support the findings of this study are available from the corresponding author upon reasonable request.

Keywords

[1] V. G. Dmitriev, G. G. Gurzadyan, D. N. Nikogosyan, *Handbook of Nonlinear Optical Crystals*, Springer Berlin Heidelberg, Berlin, Heidelberg **1997**.

[2] A. Boes, B. Corcoran, L. Chang, J. Bowers, A. Mitchell, *Laser Photonics Rev.* **2018**, *12*, 1700256.

[3] C. Wang, X. Xiong, N. Andrade, V. Venkataraman, X.-F. Ren, G.-C. Guo, M. Lončar, *Opt. Express* **2017**, *25*, 6963.

[4] L. Chang, Y. Li, N. Volet, L. Wang, J. Peters, J. E. Bowers, *Optica* **2016**, *3*, 531.

[5] R. A. Myers, N. Mukherjee, S. R. Brueck, *Opt. Lett.* **1991**, *16*, 1732.

[6] Y. Quiquempois, G. Martinelli, P. Dutherage, P. Bernage, P. Niay, M. Douay, *Opt. Commun.* **2000**, *176*, 479.

[7] Y. Quiquempois, N. Godbout, S. Lacroix, *Phys. Rev., A* **2002**, *65*, 043816.

[8] M. Dussauze, T. Cremoux, F. Adamietz, V. Rodriguez, E. Fargin, G. Yang, T. Cardinal, *Int. J. Appl. Glass Sci.* **2012**, *3*, 309.

[9] A. V. Redkov, V. G. Melehin, A. A. Lipovskii, *J. Phys. Chem. C* **2015**, *119*, 17298.

[10] A. V. Redkov, V. G. Melehin, D. V. Raskhodchikov, I. V. Reshetov, D. K. Tagantsev, V. V. Zhurikhina, A. A. Lipovskii, *J. Non-Cryst. Solids* **2018**, *503*, 279.

[11] M. Dussauze, V. Rodriguez, A. Lipovskii, M. Petrov, C. Smith, K. Richardson, T. Cardinal, E. Fargin, E. I. Kamitsos, *J. Phys. Chem. C* **2010**, *114*, 12754.

[12] F. C. Garcia, I. C. S. Carvalho, E. Hering, W. Margulis, B. Lesche, *Appl. Phys. Lett.* **1998**, *72*, 3252.

[13] P. Thamboon, D. M. Krol, *J. Appl. Phys.* **2002**, *93*, 32.

[14] P. Thamboon, D. M. Krol, *J. Appl. Phys.* **2009**, *105*, 113118.

[15] M. Dussauze, E. Fargin, M. Lahaye, V. Rodriguez, F. Adamietz, *Opt. Express* **2005**, *13*, 4064.

[16] L. Karam, F. Adamietz, V. Rodriguez, F. Bondu, A. Lepicard, T. Cardinal, E. Fargin, K. Richardson, M. Dussauze, *J. Appl. Phys.* **2020**, *128*, 043106.

[17] G. Guimbretière, M. Dussauze, V. Rodriguez, E. I. Kamitsos, *Appl. Phys. Lett.* **2010**, *97*, 171103.

[18] G. Poirier, M. Dussauze, V. Rodriguez, F. Adamietz, L. Karam, T. Cardinal, E. Fargin, *J. Phys. Chem. C* **2019**, *123*, 26528.

[19] B. Ferreira, E. Fargin, B. Guillaume, G. Le Flem, V. Rodriguez, M. Couzi, T. Buffeteau, L. Canioni, L. Sarger, G. Martinelli, Y. Quiquempois, H. Zeghlache, L. Carpentier, *J. Non-Cryst. Solids* **2003**, *332*, 207.

[20] C. Lasbrugnas, P. Thomas, O. Masson, J. C. Champarnaud-Mesjard, E. Fargin, V. Rodriguez, M. Lahaye, *Opt. Mater.* **2009**, *31*, 775.

[21] A. Narazaki, K. Tanaka, K. Hirao, N. Soga, *J. Appl. Phys.* **1999**, *85*, 2046.

[22] M. Guignard, V. Nazabal, F. Smektala, J.-L. Adam, O. Bohnke, C. Duverger, A. Moréac, H. Zeghlache, A. Kudlinski, G. Martinelli, Y. Quiquempois, *Adv. Funct. Mater.* **2007**, *17*, 3284.

[23] A. Lepicard, F. Adamietz, V. Rodriguez, K. Richardson, M. Dussauze, *Opt. Mater. Express* **2018**, *8*, 1613.

[24] M. Fokine, L. E. Nilsson, Å. Claesson, D. Berlemont, L. Kjellberg, L. Krummenacher, W. Margulis, *Opt. Lett.* **2002**, *27*, 1643.

[25] O. Tarasenko, W. Margulis, *Opt. Lett.* **2007**, *32*, 1356.

[26] J. Fage-Pedersen, R. Jacobsen, M. Kristensen, *Opt. Express* **2005**, *13*, 8514.

[27] J. Fage-Pedersen, R. Jacobsen, M. Kristensen, *J. Opt. Soc. Am. B* **2007**, *24*, 1075.

[28] G. Li, K. A. Winick, A. A. Said, M. Dugan, P. Bado, *Opt. Lett.* **2006**, *31*, 739.

[29] L. Karam, F. Adamietz, D. Michau, C. Gonçalves, M. Kang, R. Sharma, G. S. Murugan, T. Cardinal, E. Fargin, V. Rodriguez, K. A. Richardson, M. Dussauze, *Adv. Opt. Mater.* **2020**, *8*, 2000202.

[30] M. Dussauze, V. Rodriguez, F. Adamietz, G. Yang, F. Bondu, A. Lepicard, M. Chafer, T. Cardinal, E. Fargin, *Adv. Opt. Mater.* **2016**, *4*, 929.

[31] M. Dussauze, E. Fargin, A. Malakho, V. Rodriguez, T. Buffeteau, F. Adamietz, *Opt. Mater.* **2006**, *28*, 1417.

[32] Z. X. Shen, X. B. Wang, M. H. Kuok, S. H. Tang, *J. Raman Spectrosc.* **1998**, *29*, 379.

[33] F. L. Galeener, W. Stutius, G. T. McKinley, in *The Physics of MOS Insulators* (Eds: G. Lucovsky, S. T. Pantelides, F. L. Galneer), Pergamon, Oxford, UK **1980**, pp. 77–81.

[34] D. A. Kleinman, *Phys. Rev.* **1962**, *126*, 1977.

[35] T. Verbiest, K. Clays, V. Rodriguez, *Second-Order Nonlinear Optical Characterization Techniques: An Introduction*, CRC Press, Boca Raton **2009**.

[36] P. G. Kazansky, P. S. J. Russel, *Opt. Commun.* **1994**, *110*, 611.

[37] N. Bloembergen, P. S. Pershan, *Phys. Rev.* **1962**, *128*, 606.

[38] M. Iwamoto, in *Encyclopedia of Nanotechnology* (Ed: B. Bhushan), Springer Netherlands, Dordrecht **2012**, pp. 1276–1285.

[39] T. T. N. Vu, G. Teyssedre, S. L. Roy, C. Laurent, *Technologies* **2017**, *5*, 27.

[40] M. Dussauze, E. I. Kamitsos, E. Fargin, V. Rodriguez, *J. Phys. Chem. C* **2007**, *111*, 14560.

[41] V. Rodriguez, C. Sourisseau, *J. Opt. Soc. Am. B* **2002**, *19*, 2650.

[42] Q. Li, *Degree Thesis*, ENS Cachan **2014**.